

Ultrafast Heating Induced Suppression of d -band Dominance in the Electronic Excitation Spectrum of Cuprum

Zhandos Moldabekov,^{*,†,‡} Thomas D. Gawne,^{†,‡} Sebastian Schwalbe,^{†,‡}
Thomas R. Preston,[¶] Jan Vorberger,[‡] and Tobias Dornheim^{†,‡}

[†]*Center for Advanced Systems Understanding (CASUS), D-02826 Görlitz, Germany*

[‡]*Helmholtz-Zentrum Dresden-Rossendorf (HZDR), D-01328 Dresden, Germany*

[¶]*European XFEL, D-22869 Schenefeld, Germany*

E-mail: z.moldabekov@hzdr.de

Abstract

The combination of isochoric heating of solids by free electron lasers (FEL) and *in situ* diagnostics by X-ray Thomson scattering (XRTS) allows for measurements of material properties at warm dense matter (WDM) conditions relevant for astrophysics, inertial confinement fusion, and material science. In the case of metals, the FEL beam pumps energy directly into electrons with the lattice structure of ions being nearly unaffected. This leads to a unique transient state that gives rise to a set of interesting physical effects, which can serve as a reliable testing platform for WDM theories. In this work, we present extensive linear-response time-dependent density functional theory (TDDFT) results for the electronic dynamic structure factor of isochorically heated copper with a face-centered cubic lattice. At ambient conditions, the plasmon is heavily damped due to the presence of d -band excitations, and its position is independent of the

wavenumber. In contrast, the plasmon feature starts to dominate the excitation spectrum and has a Bohm-Gross type plasmon dispersion for temperatures $T \geq 4$ eV, where the quasi-free electrons in the interstitial region are in the WDM regime. In addition, we analyze the thermal changes in the d -band excitations and outline the possibility to use future XRTS measurements of isochorically heated copper as a controlled testbed for WDM theories.

1 Introduction

The study of matter under extreme densities and temperatures has emerged as a highly active research field due to the availability of modern laser facilities equipped with various X-ray diagnostic techniques. High-power laser facilities are routinely being used to explore the physics and chemistry at conditions relevant to planetary astrophysics,¹⁻³ and inertial confinement fusion,⁴⁻⁶ and to explore new exotic materials.⁷ For example, using lasers for heating and compression allows one to measure macroscopic properties such as the equation of state.⁸⁻¹³ In addition, ultrashort X-ray free electron laser (XFEL) capabilities e.g. at the European XFEL¹⁴ and LCLS¹⁵ have opened the way to study phenomena on femtosecond timescales.¹⁶ By heating the electrons without directly affecting the ions, an XFEL with a sub-100 fs duration provides a unique opportunity to generate and study a transient state with hot electrons within the unperturbed crystal structure of the ions.^{17,18} In these experiments, the X-ray Thomson scattering (XRTS) technique¹⁹ can then be used to probe the electronic structure of a given system by measuring its electronic dynamic structure factor (DSF) $S(\mathbf{q}, \omega)$, where \mathbf{q} and ω are the change in momentum and frequency of the scattered photon.

In this way, it was shown that the laser-induced heating of electrons leads to the lattice instability and melting (disordering) of silicon due to the weakening of the inter-ionic bonds.^{20,21} Another example is the laser-induced solid-solid phase transition that has been observed in bismuth.²² In contrast to semiconductors, metals can remain stable under laser

heating of the electrons, and, strikingly, can even manifest a more rigid lattice structure. For example, Descamps *et al.*¹⁷ have recently reported the observation of a stable gold crystal lattice where the electrons have been heated by the FEL to a few electronvolts. In this experiment, a signature of phonon hardening has been observed, whereby the bonds stiffen between atoms. This effect was earlier predicted by *ab initio* Kohn-Sham density functional theory (KS-DFT) calculations²³ of the hot electrons within the cold ionic lattice using the local density approximation (LDA) for the exchange–correlation (XC) functional. A second example for the successful utilization of KS-DFT for predicting the properties of solids with laser-excited electrons is the calculation of the XRTS spectrum of an isochorically heated aluminium foil by Mo *et al.*²⁴ based on linear-response time-dependent DFT (LR-TDDFT) using an adiabatic LDA (ALDA) XC kernel. The same combination of LR-TDDFT with ALDA was shown to accurately describe the XRTS spectrum of aluminum at ambient conditions, where the plasmon was measured with ultrahigh resolution at the European XFEL.²⁵ Therefore, LR-TDDFT can be expected to yield accurate results for the electronic dynamic structure factor of isochorically heated metals across temperature regimes.

Very recently, Moldabekov *et al.*²⁶ have used this approach to study the effect of electronic heating on the order of a few electronvolts on the expected XRTS spectrum;²⁶ this has revealed an interesting red shift of the plasmon energy by 0.1 eV for aluminium and by 1 eV for silicon as a consequence of thermal excitations. In the case of aluminium, the effect is small and only manifests at small wavenumbers $q \lesssim 0.1^{-1}$, making it very challenging to measure. For silicon, on the other hand, the plasmon shift of 1 eV at temperatures $T \simeq 2\text{eV}$ is well within experimental measurement capabilities.^{25,27} However, the possible instability of the lattice due to the weakening of the inter-ionic bonds^{20,21} can be a serious obstacle in practice. Therefore, it is important to ask if such a heating-induced red shift prominently manifests itself in other metals that are stable under FEL radiation. Going back to aluminium, an additional thermally induced feature is the formation of a double plasmon peak as the region of Landau damping is shifted to lower wavenumbers upon increasing the

electronic temperature.²⁶ This effect is similar to the formation of the double plasmon in the DSF of ground-state aluminum near the pair continuum.^{28–30} These results show that thermal excitations in X-ray-driven solids can generate a variety of new features in the XRTS spectrum at a finite momentum transfer.

In the present work, we carry out extensive new LR-TDDFT calculations to explore the XRTS spectrum of isochorically heated copper. In contrast to simple metals, the effect of d -states dominates over plasmon-type excitations in the DSF of electrons in transition metals.^{31,32} In gold and copper, excitations originating in the d -band lead to the formation of a prominent double peak structure at $\omega > \omega_p$ and a substantial broadening of the plasmon feature at $\omega = \omega_p$. Interestingly, the presence of the d -state excitations leads to a plasmon dispersion that is nearly independent of the wavenumber for both materials.^{31,32} Here, we investigate in detail the interplay of these effects with thermal excitations on the DSF of copper at different temperatures, wavenumbers, and crystallographic directions. Indeed, thermal effects on the DSF are profound: we find an emerging collective plasmon excitation that becomes dominant over the d -band feature for $T \gtrsim 4$ eV and which starts to follow the familiar Bohm-Gross relation in this regime. In addition, we find a pronounced blue-shift of the plasmon with increasing T , which is in stark contrast to other isochorically heated metals such as Al.²⁶ Finally, we discuss the possibility to use XRTS experiments with isochorically heated copper as a rigorous testbed for the theoretical modeling of warm dense matter (WDM)^{33–35}—an extreme state that occurs in astrophysical objects,^{3,36–38} and which plays an important role e.g. for inertial confinement fusion^{4,6,39} applications.

The paper is organized as follows: In Sec. 2, we give an overview of the LR-TDDFT approach and provide computational details of our simulations. The results of the calculations are presented and discussed in Sec. 3. The paper is concluded by a summary of the main findings and an outlook over future works in Sec. 4.

2 LR-TDDFT approach to the dynamical structure factor

2.1 Theoretical Framework

The intensity that is measured in an XRTS experiment is given by a convolution of the electronic dynamic structure factor $S(\mathbf{q}, \omega)$ with the combined source-and-instrument function $R(\omega_s)$,¹²

$$I(\mathbf{q}, \omega_s) = S(\mathbf{q}, \omega) \otimes R(\omega_s) , \quad (1)$$

where the latter accounts both for the finite width of the probing X-ray source, and for all effects of the detector.⁴⁰ The momentum transfer \mathbf{q} is determined from the scattering angle and $\omega = \omega_0 - \omega_s$ denotes the energy loss of the scattered photon where ω_0 and ω_s are the initial beam energy and the actual energy of the photon captured by the detector. The state-of-the-art is given by the European XFEL in Germany, where XRTS measurements with the capability of resolving electronic features with a resolution of up to $\Delta\omega \sim 0.1$ eV have been recently demonstrated.²⁵

To study the effect of thermal electronic excitations on the XRTS spectrum of X-ray-driven copper, we use the LR-TDDFT method with an adiabatic XC kernel. Indeed, LR-TDDFT constitutes the most common method to study the DSF of solids, and there is a vast body of dedicated literature, see e.g. Ref.⁴¹ and references therein; here, we restrict ourselves to a concise overview of the main ideas.

As a first step, we consider the well-known fluctuation–dissipation theorem that connects the macroscopic dielectric function $\epsilon_M(\mathbf{q}, \omega)$ with $S(\mathbf{q}, \omega)$,^{42,43}

$$S(\mathbf{q}, \omega) = -\frac{\hbar^2 q^2}{4\pi^2 e^2 n} \frac{1}{1 - e^{-\hbar\omega/k_B T}} \text{Im} \left[\epsilon_M^{-1}(\mathbf{q}, \omega) \right], \quad (2)$$

where n denotes the electronic number density, and e the elementary charge. The term “macroscopic” indicates that $\epsilon_M(\mathbf{q}, \omega)$ describes the volume averaged response to an external perturbation.^{44–46} It is computed by taking the diagonal part of the inverse microscopic dielectric matrix $\epsilon_M^{-1}(\mathbf{q}, \omega) = [\epsilon^{-1}(\mathbf{k}, \omega)]_{\mathbf{G}\mathbf{G}}$, where $\mathbf{q} = \mathbf{G} + \mathbf{k}$ (with \mathbf{k} being in the first Brillouin zone) and \mathbf{G} is a reciprocal lattice vector.^{47,48} The latter is defined by the microscopic density response function,⁴¹

$$\epsilon_{\mathbf{G},\mathbf{G}'}^{-1}(\mathbf{k}, \omega) = \delta_{\mathbf{G},\mathbf{G}'} + \frac{4\pi}{|\mathbf{k} + \mathbf{G}|^2} \chi_{\mathbf{G},\mathbf{G}'}(\mathbf{k}, \omega). \quad (3)$$

The LR-TDDFT method allows one to compute $\chi_{\mathbf{G},\mathbf{G}'}(\mathbf{k}, \omega)$ in different approximations. The lowest rank corresponds to the so-called independent particle approximation (IPA). In the IPA, the Kohn-Sham (KS) orbitals and eigenenergies are used to calculate the density response function $\chi_{\mathbf{G},\mathbf{G}'}^0(\mathbf{k}, \omega)$ according to the ideal electron gas model.⁴⁹ Since the KS eigenenergies from the self-consistent ground state (equilibrium state) calculations are employed, $\chi_{\mathbf{G},\mathbf{G}'}^0(\mathbf{k}, \omega)$ already has information about excitations between different orbitals. However, being computed using a formula for the ideal Fermi gas model, $\chi_{\mathbf{G},\mathbf{G}'}^0(\mathbf{k}, \omega)$ omits various correlation effects, such as screening due to the Hartree mean field, microscopic density inhomogeneities due to the field of the ions etc. The inclusion of correlation effects leads to a Dyson’s type equation for the density response function $\chi_{\mathbf{G},\mathbf{G}'}(\mathbf{k}, \omega)$:^{48,50}

$$\begin{aligned} \chi_{\mathbf{G}\mathbf{G}'}(\mathbf{k}, \omega) = & \chi_{\mathbf{G}\mathbf{G}'}^0(\mathbf{k}, \omega) + \sum_{\mathbf{G}_1\mathbf{G}_2} \chi_{\mathbf{G}\mathbf{G}_1}^0(\mathbf{k}, \omega) [v_{\mathbf{G}_1}(\mathbf{k})\delta_{\mathbf{G}_1\mathbf{G}_2} \\ & + K_{\mathbf{G}_1\mathbf{G}_2}^{\text{xc}}(\mathbf{k}, \omega)] \chi_{\mathbf{G}_2\mathbf{G}'}(\mathbf{k}, \omega), \end{aligned} \quad (4)$$

where $v_{\mathbf{G}_1}(\mathbf{k}) = 4\pi/|\mathbf{k} + \mathbf{G}_1|^2$ is the Coulomb potential in reciprocal-space, and $K_{\mathbf{G}_1,\mathbf{G}_2}^{\text{xc}}(\mathbf{k}, \omega)$ is the XC kernel capturing electronic correlations; it is defined as the functional derivative of the XC potential in KS-DFT.⁵¹

In our calculations, we have used a static (adiabatic) XC kernel $K_{\mathbf{G}_1,\mathbf{G}_2}^{\text{xc}}(\mathbf{k}, \omega = 0)$ within the ALDA.⁴¹ The ALDA is known to provide a fairly accurate description of the macroscopic dielectric function $\epsilon_M(\mathbf{q}, \omega)$ of metals and semiconductors at finite wavenumbers.^{25,30,52–54}

The relevant thermal signatures explored in this work are characterized by a difference of $\delta\omega \gtrsim 1$ eV from the ground state features. If needed, a further fine-tuning can be achieved either by employing more advanced static XC kernels beyond ALDA^{55,56} or by using an explicitly dynamic approximation (e.g., see Ref.⁵⁰ and references therein) in future works.

We note that, in the ground state, the DSF is usually studied indirectly by measuring the electronic energy loss spectrum (EELS), see, e.g., Refs.⁵⁷⁻⁵⁹ In principle, the XRTS spectrum and the EELS are directly related since

$$\text{EELS}(\mathbf{q}, \omega) = -\text{Im} [\epsilon_M^{-1}(\mathbf{q}, \omega)]. \quad (5)$$

From Eq. (2), one can see that $S(\mathbf{q}, \omega) \sim q^2 \text{EELS}(\mathbf{q}, \omega)$. This means that EELS is advantageous for measurements at small wavenumbers, whereas XRTS might be more suitable at large wavenumbers. However, EELS measurements are problematic for experiments with matter under extreme conditions due to its requirements for thin targets as well as long measurement times,⁵⁹ which are not realistic for the transient states that are of interest in the current work.

2.2 Calculation parameters

We used the GPAW code,⁶⁰⁻⁶⁵ which is a real-space implementation of the projector augmented-wave (PAW) approach.⁶⁶ We used the ground-state LDA XC-functional by Perdew and Wang.⁶⁷ The simulations have been carried out for a face-centered cubic (fcc) lattice with the lattice parameter 3.61 Å set according to the experimental value.⁶⁸ For the calculation of the KS states, we used the energy cutoff 1000 eV, the PAW dataset of copper provided by GPAW, and the primitive cell combined with the k -point grid $40 \times 40 \times 40$. We note that in the employed LR-TDDFT formalism, the momentum transfer must be the difference between two k -points times $2\pi/a$. To study the possible impact of inhomogeneity with respect to crystallographic directions on the DSF, calculations were performed along the [100], [111], and

[011] directions. We considered electronic temperatures in the range $0.025 \text{ eV} \leq T \leq 12 \text{ eV}$ and the number of KS bands was set to $N_b = 100$. The smearing of the occupation numbers was computed according to the Fermi-Dirac distribution. On the stage of the calculation of the density response matrix, the local field effect cutoff was set to 150 eV. In all calculations, we used $\eta = 0.1 \text{ eV}$ for the Lorentzian smearing parameter in $\chi_{\mathbf{G},\mathbf{G}'}(\mathbf{k},\omega)$.⁶³

3 Simulations Results

3.1 DSF $S(\mathbf{q},\omega)$ in the X-ray driven copper

We start our investigation by considering the electronic ground state (here represented by the results for $T = 0.025 \text{ eV}$) in the limit of small wave numbers. In the left panel of Fig. 1, we show the EELS spectrum at $q = 0.0754 \text{ \AA}^{-1}$ for different temperatures in the range from 0.025 eV up to 8 eV (with the temperature increasing in the subplots from bottom to top). We focus on four main features of the EELS spectrum (which equivalently appear in the DSF, cf. Fig. 4) denoted by capital letters A–D. A thorough investigation of the EELS properties of copper in the ground state has been presented by Alkauskas et al,³¹ where it was shown that features A and B are plasmon type collective oscillations, whereas C and D are a consequence of excitations between the d -band and the unoccupied states above the Fermi level. More specifically, peak B can be described as a collective plasmon oscillations of the valence electrons; this has been shown by Campillo et al³² by freezing the d -band into the core and leaving only the $4s^1$ state that forms the valence electron. Our LR-TDDFT results are in good agreement with the structure of electronic excitations reported in Refs.,^{31,32} and we reproduce the positions of all four peaks A–D.

Let us next turn to the central topic of this work, which is the study of the impact of thermal effects. With increasing the temperature, the positions of peaks B, C, and D shift to larger energies. Moreover, the amplitude of the plasmon feature B gets substantially amplified. In contrast, the signature of feature A nearly vanishes for $T \geq 2 \text{ eV}$. Compared

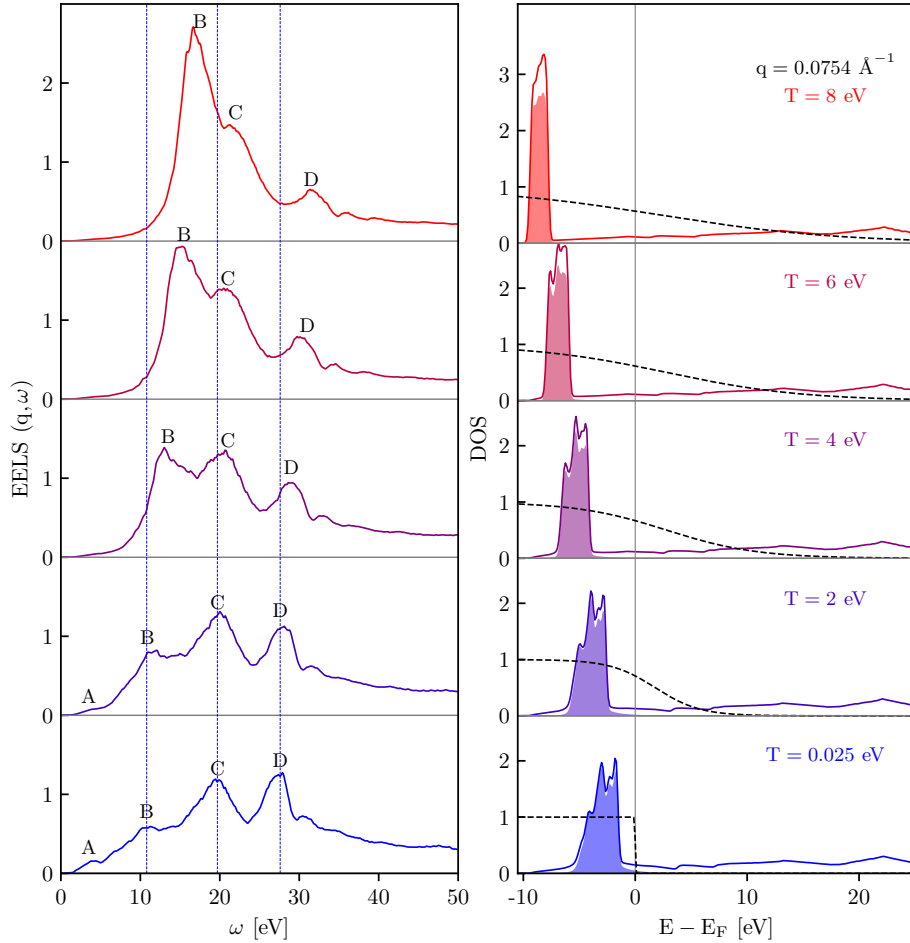


Figure 1: Left panel: EELS spectrum along the [100] direction. Right panel: total DOS (solid lines), projected DOS on d -orbital (shaded), and Fermi-Dirac occupation number distribution (dashed lines). Shown are results for $q = 0.0754 \text{ \AA}^{-1}$ at ambient conditions [$T = 0.025 \text{ eV}$], at $T = 2 \text{ eV}$, $T = 4 \text{ eV}$, $T = 6 \text{ eV}$, and at $T = 8 \text{ eV}$.

to peaks A and B, the magnitude of features C and D are only weakly affected by heating.

Following the analysis by Campillo et al³² who investigated the DSF of copper at ambient conditions, signatures B and C can be understood by considering the density of states (DOS), which is shown in the right panel of Fig. 1 as the solid lines. The d -band dominates the accumulation of the states below the Fermi energy. This is shown by the projected density of states on d -states, which is depicted by the shaded area. We find that, with increasing temperatures, the d -states are shifted to lower energies. Since the features C and D in the EELS/DSF emerge as the result of the transitions from d -states to high-lying bands above

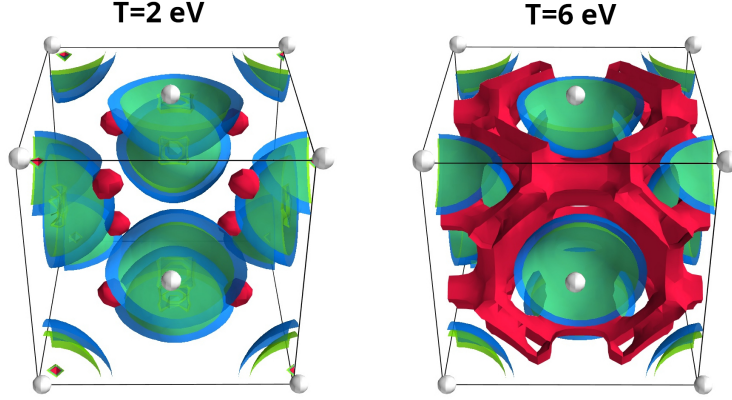


Figure 2: Electronic density accumulation in the interstitial region and density depletion around the ions due to heating at $T = 2$ eV (left) and $T = 6$ eV (right). The surface plots (semi-transparent) indicate the density change with respect to the ground state, $\delta n(\mathbf{r}) = n_T(\mathbf{r}) - n_0(\mathbf{r})$, i.e., relative to the density at $T = 0.025$ eV. The blue surface corresponds to $\delta n(\mathbf{r}) = 0$, the red surface indicates $\delta n(\mathbf{r}) = \max[\delta n(\mathbf{r})]/70 > 0$, and the green surface indicates $\delta n(\mathbf{r}) = \min[\delta n(\mathbf{r})]/15 < 0$.

the Fermi level, the observed shift of the d -states results in a blue-shift by approximately the same amount.

In addition, increasing the temperature leads to an increased number of conduction electrons, which, in turn, leads to a larger plasmon frequency, i.e., a substantial blue-shift of feature B. The corresponding increase in the electronic density in the interstitial region between the fixed ions can be demonstrated by investigating the change in the electronic density $\delta n(\mathbf{r})$ with respect to the ground state. For $T = 2$ eV ($T = 6$ eV), in atomic units, we find $\max[\delta n(\mathbf{r})] \simeq 1.45$ ($\max[\delta n(\mathbf{r})] \simeq 3.974$) and $\min[\delta n(\mathbf{r})] \simeq -0.375$ ($\min[\delta n(\mathbf{r})] \simeq -0.966$). This is illustrated in more detail in Fig. 2, where we show the thermally induced density change in the 3D simulation box for both temperatures. The blue surface depicts $\delta n(\mathbf{r}) = 0$; the red surface indicates $\delta n(\mathbf{r}) > 0$ (for the illustration, we choose $\delta n(\mathbf{r}) = \max[\delta n(\mathbf{r})]/70$); the green surface indicates $\delta n(\mathbf{r}) < 0$ (here we show $\delta n(\mathbf{r}) = \min[\delta n(\mathbf{r})]/15$). We can thus clearly see that the electronic density is reduced in the vicinity of the ions and accumulates in the interstitial region, which is more pronounced for the higher temperature, as it is expected. A more detailed, quantitative analysis of the increased free electronic density and the resulting plasmon blue-shift is presented in Sec. 3.2 below.

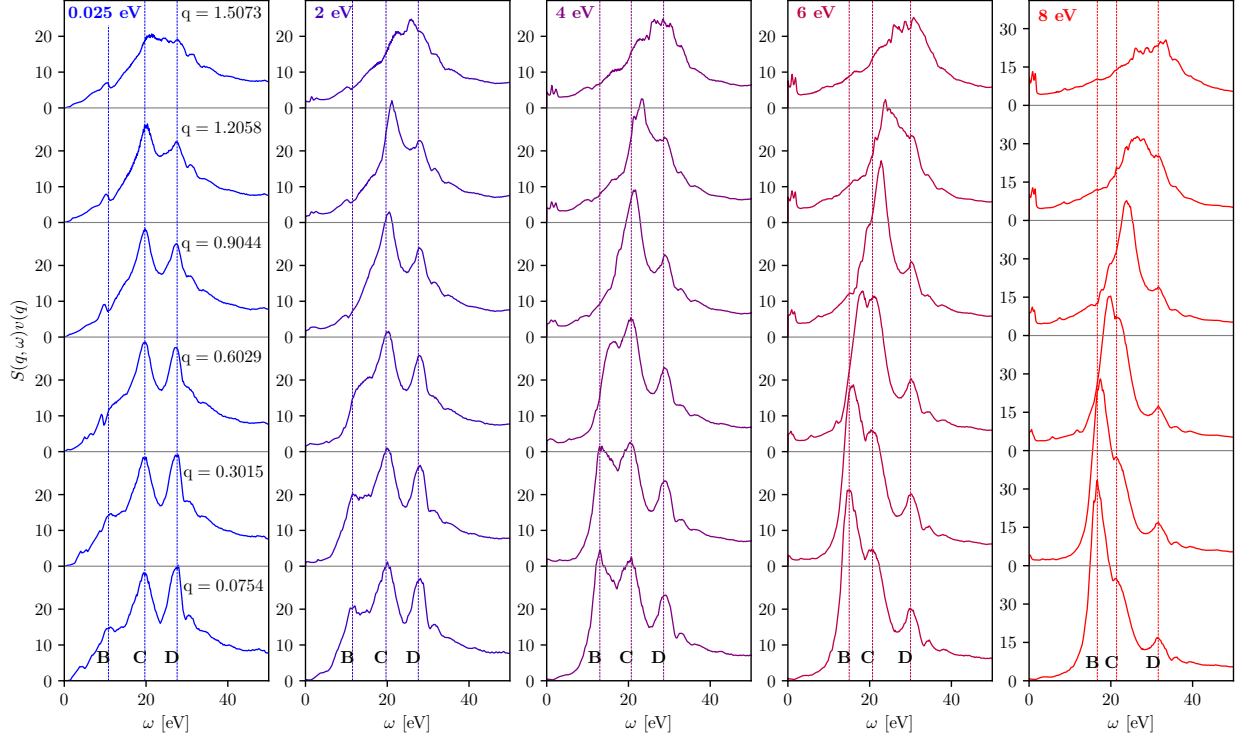


Figure 3: LR-TDDFT results for the DSF of fcc Cu along the $[100]$ direction at different wavenumbers for the ground state with $T = 0.025$ eV, and for isochorically heated electrons with $T = 2$ eV, $T = 4$ eV, $T = 6$ eV, and $T = 8$ eV. The wavenumber values are given in the units of \AA^{-1} .

Let us next investigate the DSF, which is the key property in XRTS experiments; it is shown in Fig. 3 along the $[100]$ direction for $0.0754 \text{ \AA}^{-1} \leq q \leq 1.4794 \text{ \AA}^{-1}$. Since feature A is strongly damped for $T \geq 2$ eV, we will ignore it in the following discussion and instead focus on the thermally induced changes of features B, C, and D. At all considered temperatures, the position of features C and D is nearly independent of the wavenumber. In stark contrast, the plasmon feature B exhibits a considerably richer behavior. At $T = 0.025$ eV and at $T = 2$ eV, its position does not follow the Bohm-Gross type dispersion of the free electron gas.⁴³ Overall, it is difficult to quantify its q -dependence for these two temperatures due to the comparably weak spectral weight and the possible overlap with other features due to local field effects created by the lattice structure.³¹ In contrast, we observe a pronounced increase with q for $T \geq 4$ eV. As a result, the plasmon eventually overtakes feature C, leading to the disappearance of the latter from the DSF at $q \gtrsim 0.9 \text{ \AA}^{-1}$ in the cases of $T = 4$ eV and

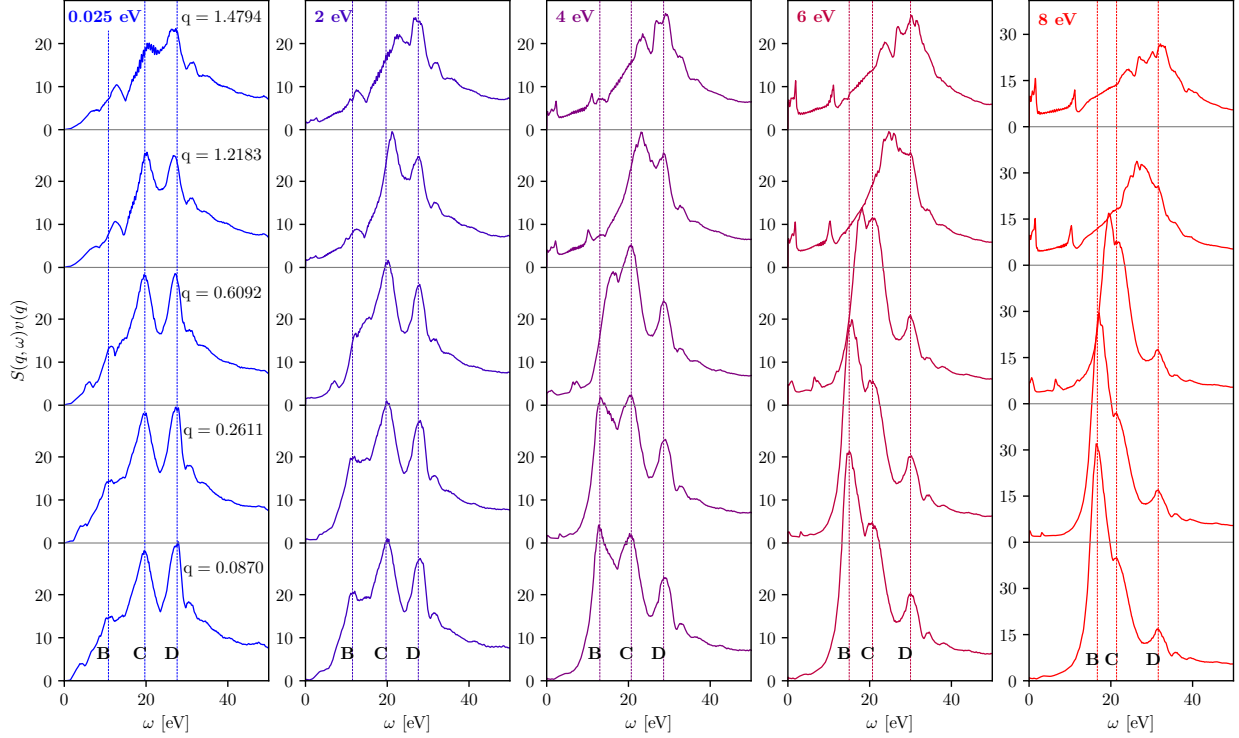


Figure 4: LR-TDDFT results for the DSF of fcc Cu along the [011] direction at different wavenumbers for the ground state with $T = 0.025$ eV, and for heated electrons with $T = 2$ eV, $T = 4$ eV, $T = 6$ eV, and $T = 8$ eV. The wavenumber values are given in the units of \AA^{-1} .

$T = 6$ eV, and at $q \gtrsim 0.6 \text{ \AA}^{-1}$ for $T = 8$ eV.

An additional interesting research topic is due to the lattice structure, which is known to lead to an anisotropy of the DSF with respect to the crystallographic direction at certain wavenumbers.^{31,69} To quantify this anisotropy effect on X-ray driven copper, we show the DSF in the [011] direction at different temperatures and wavenumbers in Fig. 4. We find that the DSF in the [011] direction closely resembles the DSF in the [100] direction for $q \lesssim 0.9 \text{ \AA}^{-1}$, and differences in the shape and peak positions emerge for $q \gtrsim 1.2 \text{ \AA}^{-1}$. For completeness, we note that the DSF in [111] direction is equivalent to the [100] direction (see Appendix). In summary, we conclude that the electronic DSF of copper is nearly isotropic at $T \geq 4$ eV for $q \lesssim 0.9 \text{ \AA}^{-1}$.

In addition to the discussed dominant features, we observe an increase in the DSF at low energies and a new peaked feature emerges in the DSF at $\omega < 10$ eV in both [100] and

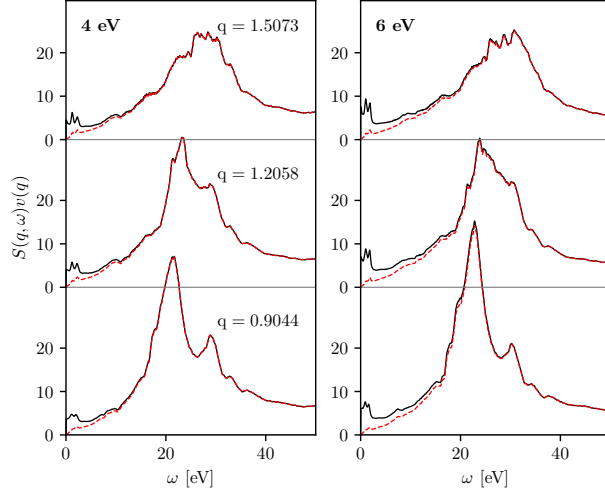


Figure 5: The demonstration of the role of the factor $f(\omega) = (1 - e^{-\hbar\omega/k_B T})^{-1}$ on the enhancement of the DSF features at small energies. Solid lines are the results for the DSF along the [100] direction and dashed lines are the same data divided by $f(\omega)$.

[011] directions at $T \geq 4$ eV and $q \gtrsim 0.6$ Å⁻¹. The increase in the temperature modifies the DSF due to the factor $f(\omega) = (1 - e^{-\hbar\omega/k_B T})^{-1}$ in Eq. (2). This effect is particularly pronounced for the low-energy part of the DSF, and enhances subtle features in this regime. This is illustrated in Fig. 5 for $T = 4$ eV and $T = 6$ eV at wavenumbers $q = 0.9044$ Å⁻¹, $q = 1.2058$ Å⁻¹, and $q = 1.5073$ Å⁻¹. From Fig. 5 we observe that the factor $f(\omega)$ in Eq. (2) for the DSF results in the substantial increase of the DSF values at low energies leading to an amplification of the thermally induced features at $\omega < 10$ eV. Physically, these features might originate from transitions between accumulated states located closely above the Fermi level, cf. Fig. 1. Indeed, one can observe that at $T \geq 4$ eV states above the Fermi level become partially occupied allowing the emergence of new excitation features.

3.2 Plasmon dispersion and conditions in interstitial regions

Analyzing the DSF, we have found that the collective plasmon oscillations in X-ray driven copper overcome the dominance of the d -band excitations, eventually overtaking them with respect to the spectral weight. In addition, the plasmon position starts to exhibit a substantial dispersion with respect to the wavenumber for sufficiently high temperatures, which is in

contrast to the ground state plasmon. To examine the character of the plasmon dispersion, we show the dependence of the plasmon energy (frequency) on the wavenumber, $\omega(q)$, in Fig. 6 for different temperatures. We consider $q < 1 \text{ \AA}^{-1}$, where the plasmon peak can be clearly identified at all considered temperatures, and independent of the crystallographic direction. The uncertainty in the plasmon position is evaluated by looking at the onset of a broadened peak. At $T = 2 \text{ eV}$, we find that $\omega(q)$ is qualitatively similar to the results for $T = 0.025 \text{ eV}$. For $T \geq 4 \text{ eV}$, the plasmon dispersion starts to follow the familiar quadratic dependence on q that is well-known from the free electron gas model.⁷⁰ To further quantify this trend, we fit the LR-TDDFT results using the Bohm-Gross type dispersion relation,^{71,72}

$$\omega^2(q) = \omega_p^2 + \alpha q^2, \quad (6)$$

where α and ω_p are the free parameters. The results are shown as the solid ([011] direction) and dashed ([100] direction) lines in Fig. 6, which are nearly identical; the small differences are likely due to uncertainties introduced by the broadened peaks of the DSF.

In subsection 3.1, we have indicated that the increase in the plasmon energy with the temperature is a consequence of the excess electronic density in the interstitial regions between the ionic lattice, cf. Fig. 2. Here, we propose to utilize such forward scattering data for the DSF as a diagnostic for the free electronic density and for the effective charge state. Specifically, we define the effective density parameter \tilde{r}_s by inverting the usual relation between the density and the plasmon frequency of a free electron gas,

$$\omega_p = \left(4\pi\tilde{n} \frac{e^2}{m_e} \right)^{1/2} \Rightarrow \tilde{r}_s = \left(\frac{3}{4\pi} \tilde{n} \right)^{1/3}. \quad (7)$$

We note that the parameter \tilde{r}_s also characterizes the coupling strength or, equivalently, the degree of non-ideality of the free electrons.^{34,73}

An additional, related effective parameter of interest is given by the corresponding degeneracy temperature $\tilde{\Theta} = k_B T / E_F(\tilde{n})$, where $E_F(\tilde{n}) = (3\pi^2\tilde{n})^{1/3}$ denotes the Fermi energy

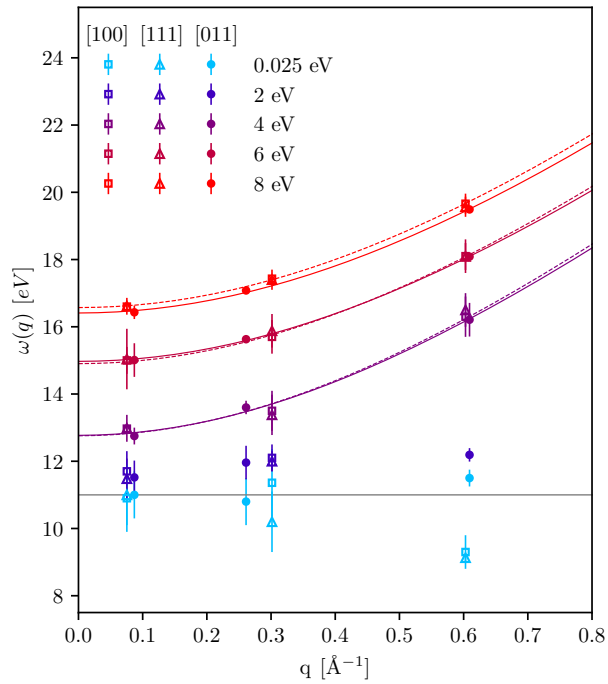


Figure 6: Dependence of the plasmon frequency on the wavenumber along different crystallographic directions at $T = 0.025$ eV, $T = 2$ eV, $T = 4$ eV, $T = 6$ eV, and $T = 8$ eV. Solid (dashed) lines show Bohm-Gross type quadratic dispersion fits [cf. Eq. (6)] for the direction [111] ([100]) at $T = 4$ eV, $T = 6$ eV, and $T = 8$ eV. The horizontal solid grey line at 10.864 eV indicates the plasmon energy computed using the free electron gas model, i.e., assigning the $3d$ shell as a core state.³²

of a free electron gas of density \tilde{n} .⁴³ Finally, we consider the effective ionic charge \tilde{Z} , which is a key ingredient to equation-of-state tables.^{9,10} The effective charge is computed using $\tilde{Z} = (\tilde{r}_s(T=0)/\tilde{r}_s(T))^3$, which follows from the condition $\tilde{Z}n_i = \tilde{n}$, with $n_i = \text{const}$ being the number density of ions, and setting $Z = 1$ for copper at $T = 0$ since we have one valence electron in the 4s state.

In Table 1, we provide an overview of these parameters for all selected temperatures. For $T = 0.025$ eV, we find an effective density parameter of $\tilde{r}_s = 2.64 \pm 0.11$, which agrees with the value $r_s = 2.668$ that corresponds to the conduction electrons density in the fcc copper at room temperature.

Upon increasing the temperature, we find a monotonic increase in the density of effectively free electrons, leading to a corresponding decrease of \tilde{r}_s and an increase in \tilde{Z} . The observed monotonic increase of $\tilde{\Theta}$ is less trivial. On the one hand, we have $\tilde{\Theta} \sim \tilde{r}_s^2$,⁷³ which, by itself, would indicate a decrease of $\tilde{\Theta}$ with T . However, this effect is overridden by the relation $\tilde{\Theta} \sim T$ in practice.

Table 1 clearly shows that the effectively free electrons in the interstitial region of isochorically heated copper are in the WDM regime.³³ In nature, WDM occurs in a variety of astrophysical objects such as giant planet interiors,³ brown dwarfs,³⁷ and white dwarf atmospheres.³⁶ In the laboratory, these conditions are encountered on the compression path of a fuel capsule and its ablator in inertial confinement fusion experiments,^{4,6,39} and, in addition, they are relevant for material science, synthesis, and discovery.^{74,75} Despite its fundamental importance for a gamut of applications, the rigorous theoretical description of WDM remains challenging: it must cover the complex interplay between effects such as partial ionization, Coulomb coupling, and quantum degeneracy and diffraction, which is notoriously difficult in practice.³³⁻³⁵ Our new simulation results thus imply that future XRTS experiments with isochorically heated copper constitute a suitable and highly controlled testbed for the benchmarking of theoretical methods and simulations.

Table 1: Plasmon energy at $q = 0.0754 \text{ \AA}^{-1}$ extracted from the DSF calculations with corresponding effective density parameter \tilde{r}_s , effective degeneracy parameter $\tilde{\Theta}$, and effective charge of ions \tilde{Z} .

T [eV]	ω_p [eV]	\tilde{r}_s	$\tilde{\Theta}$	\tilde{Z}
0.025	11 ± 0.7	2.64 ± 0.11	0	1.0 ± 0.06
2	11.52 ± 0.5	2.56 ± 0.07	0.261 ± 0.01	1.1 ± 0.09
4	12.75 ± 0.25	2.39 ± 0.03	0.456 ± 0.01	1.34 ± 0.14
6	15.01 ± 0.5	2.14 ± 0.04	0.551 ± 0.02	1.86 ± 0.17
8	16.43 ± 0.2	2.02 ± 0.02	0.651 ± 0.01	2.23 ± 0.25
10	18.3 ± 0.4	1.88 ± 0.027	0.704 ± 0.02	2.77 ± 0.29
12	19.43 ± 0.35	1.80 ± 0.02	0.780 ± 0.019	3.12 ± 0.33

4 Conclusions

Motivated by experimental capabilities at modern FEL facilities, we have performed a detailed study of the changes in the electronic DSF in fcc copper due to isochoric heating. Our new LR-TDDFT simulations show that the heating induces a prominent plasmon feature that eventually becomes dominant over the d -band-signal. This is in marked contrast to the ground state, where the plasmon is strongly damped by the presence of d -band excitations, and where it does not exhibit a meaningful dispersion with respect to the wavenumber q . Indeed, we have shown that at $T \geq 4$ eV, the plasmon dispersion follows the familiar Bohm-Gross type relation, and the plasma frequency ω_p substantially increases with the temperature. This has been explained by the accumulation of effectively free electrons in the interstitial region between the ions. This, in turn, is a consequence of the availability of the electrons in the d -orbitals for filling states in the quasicontinuum when the temperature is increased. Interestingly, the reported behavior of the plasmon in copper is fundamentally different from isochorically heated aluminium, where LR-TDDFT simulations have shown that heating to a few electronvolts (at $T \lesssim 7$ eV) causes a red shift of ω_p .²⁶

From a physical perspective, we find that the quasi-free electrons in the interstitial space

are in the WDM regime with an effective density parameter $\tilde{r}_s \sim 2$ and an effective degeneracy temperature $\tilde{\Theta} \sim 0.5$. In addition to being interesting in their own right, such extreme conditions occur in a wealth of astrophysical objects and play a key role in experiments with inertial confinement fusion and material science. In practice, there does not exist a single method that is capable of giving an accurate description of WDM states over the entire relevant parameter space, and the interpretation, modeling, and design of corresponding experiments is usually based on a number of de-facto uncontrolled approximations.

In this regard, we propose to use future XRTS experiments with isochorically heated copper as a controlled testbed for the rigorous assessment of different theoretical models and simulation tools for the description of WDM. Ideally, one might infer the temperature of the heated sample based on the model-free imaginary-time thermometry approach^{11,12} as a first step. Indeed, even the inference of comparably moderate temperatures of $T \sim 1 - 10$ eV is expected to be feasible using the new high-resolution set-up that has recently been demonstrated at the European XFEL in Germany.²⁵ Second, we propose to carry out measurements at multiple scattering angles (i.e., multiple wavenumbers q) to observe the plasmon dispersion $\omega(q)$ and, in this way, to infer the effective charge state \tilde{Z} and the effective density parameter \tilde{r}_s . Since the ambient density is a-priori known, this will give one full access to the most relevant parameters of the system. This is an important advantage over shock experiments, or XRTS measurements with backlighter sources,⁴⁰ where one or multiple of these parameters can only be inferred on the basis of the theoretical models which we aim to test in the first place.

Such a hypothetical XRTS dataset can then be used to benchmark the zoo of available theoretical methods such as the widely used effective chemical models.^{19,76,77} A particularly interesting question is the assessment of XC functionals in KS-DFT simulations, including the resolution of explicitly thermal XC effects.⁷⁸⁻⁸⁴ Moreover, frequency-resolved inelastic X-ray scattering data for a set of finite wavenumbers q will be ideally suited to gauge the accuracy of different XC-kernels in LR-TDDFT calculations, including a rigorous assessment

of the popular adiabatic approximation.^{41,45,85}

Acknowledgments

This work was partially supported by the Center for Advanced Systems Understanding (CASUS), financed by Germany's Federal Ministry of Education and Research (BMBF) and the Saxon state government out of the State budget approved by the Saxon State Parliament. This work has received funding from the European Union's Just Transition Fund (JTF) within the project Röntgenlaser-Optimierung der Laserfusion (ROLF), contract number 5086999001, co-financed by the Saxon state government out of the State budget approved by the Saxon State Parliament. This work has received funding from the European Research Council (ERC) under the European Union's Horizon 2022 research and innovation programme (Grant agreement No. 101076233, "PREXTREME"). Views and opinions expressed are however those of the authors only and do not necessarily reflect those of the European Union or the European Research Council Executive Agency. Neither the European Union nor the granting authority can be held responsible for them. Computations were performed on a Bull Cluster at the Center for Information Services and High-Performance Computing (ZIH) at Technische Universität Dresden, at the Norddeutscher Verbund für Hoch- und Höchstleistungsrechnen (HLRN) under grant mvp00024, and on the HoreKa supercomputer funded by the Ministry of Science, Research and the Arts Baden-Württemberg and by the Federal Ministry of Education and Research.

Appendix

For completeness, we show the DSF in the [111] direction at the different considered temperatures and wavenumbers in Fig. 7. We find that the B, C, and D features behave similarly to our results for the [100] and [111] directions, both with respect to temperature and wavenumber. Indeed, the DSF in [111] direction is nearly identical to the DSF in [100] direction over

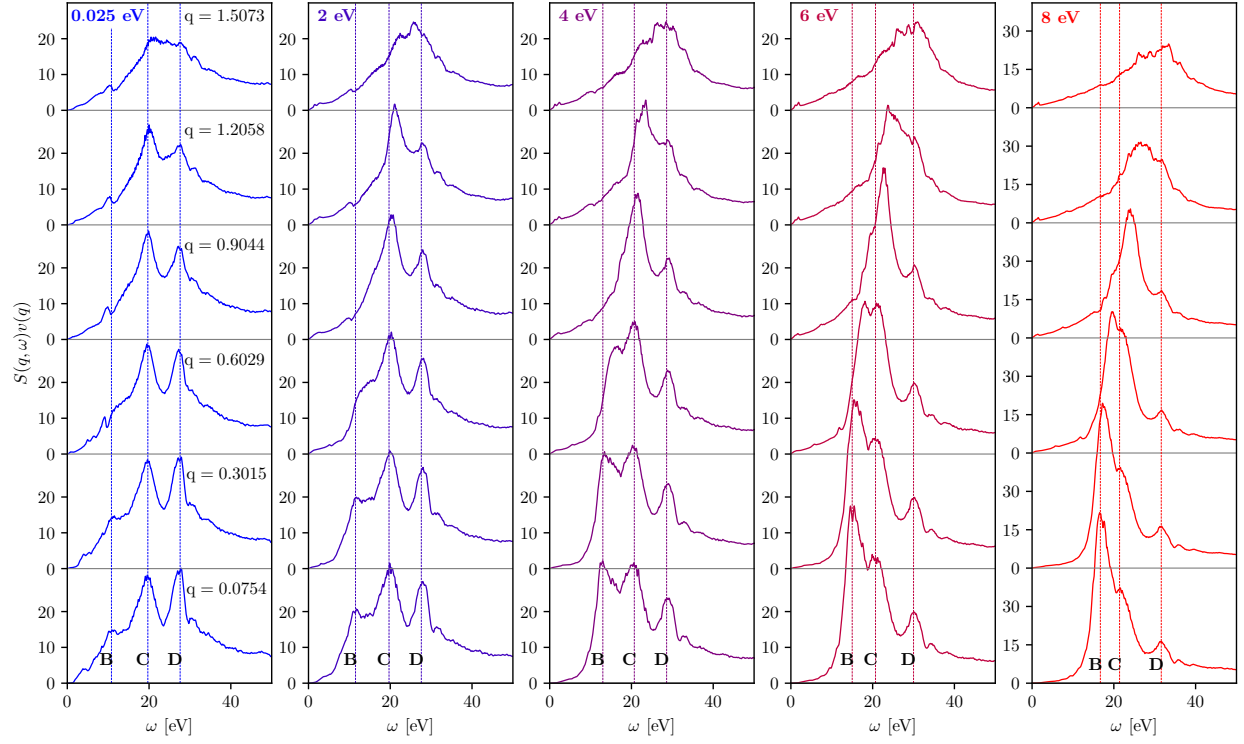


Figure 7: LR-TDDFT results for the DSF of fcc Cu along the [111] direction at different wavenumbers for the ground state with $T = 0.025$ eV, and for heated electrons with $T = 2$ eV, $T = 4$ eV, $T = 6$ eV, and $T = 8$ eV. The wavenumber values are given in the units of \AA^{-1} .

the entire depicted q -range.

References

- (1) Millot, M.; Hamel, S.; Rygg, J. R.; Celliers, P. M.; Collins, G. W.; Coppari, F.; Fratanduono, D. E.; Jeanloz, R.; Swift, D. C.; Eggert, J. H. Experimental evidence for superionic water ice using shock compression. Nature Physics **2018**, 14, 297–302.
- (2) Morales, M. A.; Pierleoni, C.; Schwegler, E.; Ceperley, D. M. Evidence for a first-order liquid-liquid transition in high-pressure hydrogen from ab initio simulations. Proceedings of the National Academy of Sciences **2010**, 107, 12799–12803.
- (3) Benuzzi-Mounaix, A.; Mazevet, S.; Ravasio, A.; Vinci, T.; Denoëud, A.; Koenig, M.; Amadou, N.; Brambrink, E.; Festa, F.; Levy, A.; Harmand, M.; Brygoo, S.; Huser, G.; Recoules, V.; Bouchet, J.; Morard, G.; Guyot, F.; de Resseguier, T.; Myanishi, K.; Ozaki, N.; Dorchie, F.; Gaudin, J.; Leguay, P. M.; Peyrusse, O.; Henry, O.; Raffestin, D.; Pape, S. L.; Smith, R.; Musella, R. Progress in warm dense matter study with applications to planetology. Phys. Scripta **2014**, T161, 014060.
- (4) Hu, S. X.; Militzer, B.; Goncharov, V. N.; Skupsky, S. First-principles equation-of-state table of deuterium for inertial confinement fusion applications. Phys. Rev. B **2011**, 84, 224109.
- (5) Fernandez-Pañella, A.; Millot, M.; Fratanduono, D. E.; Desjarlais, M. P.; Hamel, S.; Marshall, M. C.; Erskine, D. J.; Sterne, P. A.; Haan, S.; Boehly, T. R.; Collins, G. W.; Eggert, J. H.; Celliers, P. M. Shock Compression of Liquid Deuterium up to 1 TPa. Phys. Rev. Lett. **2019**, 122, 255702.
- (6) Betti, R. A milestone in fusion research is reached. Nature Reviews Physics **2023**, 5, 6–8.

- (7) Miao, M.; Sun, Y.; Zurek, E.; Lin, H. Chemistry under high pressure. Nature Reviews Chemistry **2020**, 4, 508–527.
- (8) Regan, S. P.; Falk, K.; Gregori, G.; Radha, P. B.; Hu, S. X.; Boehly, T. R.; Crowley, B. J. B.; Glenzer, S. H.; Landen, O. L.; Gericke, D. O.; Döppner, T.; Meyerhofer, D. D.; Murphy, C. D.; Sangster, T. C.; Vorberger, J. Inelastic X-Ray Scattering from Shocked Liquid Deuterium. Phys. Rev. Lett. **2012**, 109, 265003.
- (9) Falk, K.; Gamboa, E. J.; Kagan, G.; Montgomery, D. S.; Srinivasan, B.; Tzeferacos, P.; Benage, J. F. Equation of State Measurements of Warm Dense Carbon Using Laser-Driven Shock and Release Technique. Phys. Rev. Lett. **2014**, 112, 155003.
- (10) Döppner, T.; Bethkenhagen, M.; Kraus, D.; Neumayer, P.; Chapman, D. A.; Bachmann, B.; Baggett, R. A.; Böhme, M. P.; Divol, L.; Falcone, R. W.; Fletcher, L. B.; Landen, O. L.; MacDonald, M. J.; Saunders, A. M.; Schörner, M.; Sterne, P. A.; Vorberger, J.; Witte, B. B. L.; Yi, A.; Redmer, R.; Glenzer, S. H.; Gericke, D. O. Observing the onset of pressure-driven K-shell delocalization. Nature **2023**,
- (11) Dornheim, T.; Böhme, M.; Kraus, D.; Döppner, T.; Preston, T. R.; Moldabekov, Z. A.; Vorberger, J. Accurate temperature diagnostics for matter under extreme conditions. Nature Communications **2022**, 13, 7911.
- (12) Dornheim, T.; Böhme, M. P.; Chapman, D. A.; Kraus, D.; Preston, T. R.; Moldabekov, Z. A.; Schlünzen, N.; Cangi, A.; Döppner, T.; Vorberger, J. Imaginary-time correlation function thermometry: A new, high-accuracy and model-free temperature analysis technique for x-ray Thomson scattering data. Physics of Plasmas **2023**, 30, 042707.
- (13) Dornheim, T.; Döppner, T.; Talias, P.; Böhme, M.; Fletcher, L.; Gawne, T.; Graziani, F.; Kraus, D.; MacDonald, M.; Moldabekov, Z.; Schwalbe, S.; Gericke, D.; Vorberger, J. Unraveling electronic correlations in warm dense quantum plasmas. 2024.

- (14) Zastra, U.; Appel, K.; Baehtz, C.; Baehr, O.; Batchelor, L.; Berghäuser, A.; Banjafar, M.; Brambrink, E.; Cerantola, V.; Cowan, T. E.; Damker, H.; Dietrich, S.; Di Dio Cafiso, S.; Dreyer, J.; Engel, H.-O.; Feldmann, T.; Findeisen, S.; Foese, M.; Fulla-Marsa, D.; Göde, S.; Hassan, M.; Hauser, J.; Herrmannsdörfer, T.; Höppner, H.; Kaa, J.; Kaefer, P.; Knöfel, K.; Konôpková, Z.; Laso García, A.; Liermann, H.-P.; Mainberger, J.; Makita, M.; Martens, E.-C.; McBride, E. E.; Möller, D.; Nakatsutsumi, M.; Pelka, A.; Plueckthun, C.; Prescher, C.; Preston, T. R.; Röper, M.; Schmidt, A.; Seidel, W.; Schwinkendorf, J.-P.; Schoelmerich, M. O.; Schramm, U.; Schropp, A.; Strohm, C.; Sukharnikov, K.; Talkovski, P.; Thorpe, I.; Toncian, M.; Toncian, T.; Wollenweber, L.; Yamamoto, S.; Tschentscher, T. The High Energy Density Scientific Instrument at the European XFEL. Journal of Synchrotron Radiation **2021**, 28, 1393–1416.
- (15) Fletcher, L. B.; Lee, H. J.; Döppner, T.; Galtier, E.; Nagler, B.; Heimann, P.; Fortmann, C.; LePape, S.; Ma, T.; Millot, M.; Pak, A.; Turnbull, D.; Chapman, D. A.; Gericke, D. O.; Vorberger, J.; White, T.; Gregori, G.; Wei, M.; Barbrel, B.; Falcone, R. W.; Kao, C.-C.; Nuhn, H.; Welch, J.; Zastra, U.; Neumayer, P.; Hastings, J. B.; Glenzer, S. H. Ultrabright X-ray laser scattering for dynamic warm dense matter physics. Nature Photonics **2015**, 9, 274–279.
- (16) Vorberger, J.; Preston, T. R.; Medvedev, N.; Böhme, M. P.; Moldabekov, Z. A.; Kraus, D.; Dornheim, T. Revealing non-equilibrium and relaxation in laser heated matter. Physics Letters A **2024**, 499, 129362.
- (17) Descamps, A.; Ofori-Okai, B. K.; Bistoni, O.; Chen, Z.; Cunningham, E.; Fletcher, L. B.; Hartley, N. J.; Hastings, J. B.; Khaghani, D.; Mo, M.; Nagler, B.; Recoules, V.; Redmer, R.; Schörner, M.; Senesky, D. G.; Sun, P.; Tsai, H.-E.; White, T. G.; Glenzer, S. H.; McBride, E. E. Evidence for phonon hardening in laser-excited gold us-

- ing x-ray diffraction at a hard x-ray free electron laser. Science Advances **2024**, 10, eadh5272.
- (18) Descamps, A.; Ofori-Okai, B. K.; Appel, K.; Cerantola, V.; Comley, A.; Eggert, J. H.; Fletcher, L. B.; Gericke, D. O.; Göde, S.; Humphries, O.; Karnbach, O.; Lazicki, A.; Loetzsch, R.; McGonegle, D.; Palmer, C. A. J.; Plueckthun, C.; Preston, T. R.; Redmer, R.; Senesky, D. G.; Strohm, C.; Uschmann, I.; White, T. G.; Wollenweber, L.; Monaco, G.; Wark, J. S.; Hastings, J. B.; Zastrau, U.; Gregori, G.; Glenzer, S. H.; McBride, E. E. An approach for the measurement of the bulk temperature of single crystal diamond using an X-ray free electron laser. Scientific Reports **2020**, 10, 14564.
- (19) Glenzer, S. H.; Redmer, R. X-ray Thomson scattering in high energy density plasmas. Rev. Mod. Phys **2009**, 81, 1625.
- (20) Biswas, R.; Ambegaokar, V. Phonon spectrum of a model of electronically excited silicon. Phys. Rev. B **1982**, 26, 1980–1988.
- (21) Recoules, V.; Clérouin, J.; Zérah, G.; Anglade, P. M.; Mazevet, S. Effect of Intense Laser Irradiation on the Lattice Stability of Semiconductors and Metals. Phys. Rev. Lett. **2006**, 96, 055503.
- (22) Sokolowski-Tinten, K.; Blome, C.; Blums, J.; Cavalleri, A.; Dietrich, C.; Tarasevitch, A.; Uschmann, I.; Förster, E.; Kammler, M.; Horn-von Hoegen, M.; von der Linde, D. Femtosecond X-ray measurement of coherent lattice vibrations near the Lindemann stability limit. Nature **2003**, 422, 287–289.
- (23) Recoules, V.; Clérouin, J.; Zérah, G.; Anglade, P. M.; Mazevet, S. Effect of Intense Laser Irradiation on the Lattice Stability of Semiconductors and Metals. Phys. Rev. Lett. **2006**, 96, 055503.
- (24) Mo, C.; Fu, Z.; Kang, W.; Zhang, P.; He, X. T. First-Principles Estimation of Electronic

- Temperature from X-Ray Thomson Scattering Spectrum of Isochorically Heated Warm Dense Matter. Phys. Rev. Lett. **2018**, 120, 205002.
- (25) Gawne, T.; Moldabekov, Z. A.; Humphries, O. S.; Appel, K.; Bächtz, C.; Bouffetier, V.; Brambrink, E.; Cangi, A.; Göde, S.; Konôpková, Z.; Makita, M.; Mishchenko, M.; Nakatsutsumi, M.; Ramakrishna, K.; Randolph, L.; Schwalbe, S.; Vorberger, J.; Wollenweber, L.; Zastra, U.; Dornheim, T.; Preston, T. R. Ultrahigh Resolution X-ray Thomson Scattering Measurements of Electronic Structures. 2024.
- (26) Moldabekov, Z. A.; Gawne, T. D.; Schwalbe, S.; Preston, T. R.; Vorberger, J.; Dornheim, T. Excitation signatures of isochorically heated electrons in solids at finite wavenumber explored from first principles. 2024.
- (27) Wollenweber, L.; Preston, T. R.; Descamps, A.; Cerantola, V.; Comley, A.; Eggert, J. H.; Fletcher, L. B.; Geloni, G.; Gericke, D. O.; Glenzer, S. H.; Göde, S.; Hastings, J.; Humphries, O. S.; Jenei, A.; Karnbach, O.; Konopkova, Z.; Loetzsch, R.; Marx-Glowna, B.; McBride, E. E.; McGonegle, D.; Monaco, G.; Ofori-Okai, B. K.; Palmer, C. A. J.; Plückthun, C.; Redmer, R.; Strohm, C.; Thorpe, I.; Tschentscher, T.; Uschmann, I.; Wark, J. S.; White, T. G.; Appel, K.; Gregori, G.; Zastra, U. High-resolution inelastic x-ray scattering at the high energy density scientific instrument at the European X-Ray Free-Electron Laser. Review of Scientific Instruments **2021**, 92, 013101.
- (28) Schülke, W.; Schulte-Schrepping, H.; Schmitz, J. R. Dynamic structure of electrons in Al metal studied by inelastic x-ray scattering. Phys. Rev. B **1993**, 47, 12426–12436.
- (29) Larson, B.; Tischler, J.; Fleszar, A.; Eguluz, A. Correlation and band structure effects in the electronic energy loss spectra of Al: an experimental perspective. Journal of Physics and Chemistry of Solids **2000**, 61, 391–396.
- (30) Cazzaniga, M.; Weissker, H.-C.; Huotari, S.; Pylkkänen, T.; Salvestrini, P.; Monaco, G.;

- Onida, G.; Reining, L. Dynamical response function in sodium and aluminum from time-dependent density-functional theory. Phys. Rev. B **2011**, 84, 075109.
- (31) Alkauskas, A.; Schneider, S. D.; Hébert, C.; Sagmeister, S.; Draxl, C. Dynamic structure factors of Cu, Ag, and Au: Comparative study from first principles. Phys. Rev. B **2013**, 88, 195124.
- (32) Campillo, I.; Rubio, A.; Pitarke, J. M. Ab initio calculations of the dynamical response of copper. Phys. Rev. B **1999**, 59, 12188–12191.
- (33) Graziani, F., Desjarlais, M. P., Redmer, R., Trickey, S. B., Eds. Frontiers and Challenges in Warm Dense Matter; Springer: International Publishing, 2014.
- (34) Bonitz, M.; Dornheim, T.; Moldabekov, Z. A.; Zhang, S.; Hamann, P.; Kählert, H.; Filinov, A.; Ramakrishna, K.; Vorberger, J. Ab initio simulation of warm dense matter. Physics of Plasmas **2020**, 27, 042710.
- (35) Dornheim, T.; Moldabekov, Z. A.; Ramakrishna, K.; Tolias, P.; Baczewski, A. D.; Kraus, D.; Preston, T. R.; Chapman, D. A.; Böhme, M. P.; Döppner, T.; Graziani, F.; Bonitz, M.; Cangi, A.; Vorberger, J. Electronic density response of warm dense matter. Physics of Plasmas **2023**, 30, 032705.
- (36) Kritcher, A. L.; Swift, D. C.; Döppner, T.; Bachmann, B.; Benedict, L. X.; Collins, G. W.; DuBois, J. L.; Elsner, F.; Fontaine, G.; Gaffney, J. A.; Hamel, S.; Lazicki, A.; Johnson, W. R.; Kostinski, N.; Kraus, D.; MacDonald, M. J.; Maddox, B.; Martin, M. E.; Neumayer, P.; Nikroo, A.; Nilsen, J.; Remington, B. A.; Saumon, D.; Sterne, P. A.; Sweet, W.; Correa, A. A.; Whitley, H. D.; Falcone, R. W.; Glenzer, S. H. A measurement of the equation of state of carbon envelopes of white dwarfs. Nature **2020**, 584, 51–54.
- (37) Becker, A.; Lorenzen, W.; Fortney, J. J.; Nettelmann, N.; Schöttler, M.; Redmer, R. Ab initio equations of state for hydrogen (H-REOS.3) and helium (He-REOS.3) and

- their implications for the interior of brown dwarfs. *Astrophys. J. Suppl. Ser* **2014**, 215, 21.
- (38) Fortov, V. E. Extreme states of matter on Earth and in space. *Phys.-Usp* **2009**, 52, 615–647.
- (39) Betti, R.; Hurricane, O. A. Inertial-confinement fusion with lasers. *Nature Physics* **2016**, 12, 435–448.
- (40) MacDonald, M. J.; Saunders, A. M.; Bachmann, B.; Bethkenhagen, M.; Divol, L.; Doyle, M. D.; Fletcher, L. B.; Glenzer, S. H.; Kraus, D.; Landen, O. L.; LeFevre, H. J.; Klein, S. R.; Neumayer, P.; Redmer, R.; Schörner, M.; Whiting, N.; Falcone, R. W.; Döppner, T. Demonstration of a laser-driven, narrow spectral bandwidth x-ray source for collective x-ray scattering experiments. *Physics of Plasmas* **2021**, 28, 032708.
- (41) Ullrich, C. A. *Time-Dependent Density-Functional Theory: Concepts and Applications*; Oxford University Press, 2011.
- (42) Kubo, R. The fluctuation-dissipation theorem. *Reports on Progress in Physics* **1966**, 29, 255.
- (43) Giuliani, G.; Vignale, G. *Quantum Theory of the Electron Liquid*; Cambridge University Press: Cambridge, 2008.
- (44) Gurtubay, I. G.; Pitarke, J. M.; Ku, W.; Eguiluz, A. G.; Larson, B. C.; Tischler, J.; Zschack, P.; Finkelstein, K. D. Electron-hole and plasmon excitations in 3d transition metals: Ab initio calculations and inelastic x-ray scattering measurements. *Phys. Rev. B* **2005**, 72, 125117.
- (45) Moldabekov, Z. A.; Pavanello, M.; Böhme, M. P.; Vorberger, J.; Dornheim, T. Linear-response time-dependent density functional theory approach to warm dense matter with adiabatic exchange-correlation kernels. *Phys. Rev. Res.* **2023**, 5, 023089.

- (46) Moldabekov, Z. A.; Vorberger, J.; Lokamani, M.; Dornheim, T. Averaging over atom snapshots in linear-response TDDFT of disordered systems: A case study of warm dense hydrogen. The Journal of Chemical Physics **2023**, 159, 014107.
- (47) Gurtubay, I. G.; Pitarke, J. M.; Ku, W.; Eguiluz, A. G.; Larson, B. C.; Tischler, J.; Zschack, P.; Finkelstein, K. D. Electron-hole and plasmon excitations in 3d transition metals: Ab initio calculations and inelastic x-ray scattering measurements. Phys. Rev. B **2005**, 72, 125117.
- (48) Martin, R. M.; Reining, L.; Ceperley, D. M. Interacting Electrons: Theory and Computational Approaches; Cambridge University Press, 2016.
- (49) Hybertsen, M. S.; Louie, S. G. Ab initio static dielectric matrices from the density-functional approach. I. Formulation and application to semiconductors and insulators. Phys. Rev. B **1987**, 35, 5585–5601.
- (50) Byun, Y.-M.; Sun, J.; Ullrich, C. A. Time-dependent density-functional theory for periodic solids: assessment of excitonic exchange–correlation kernels. Electronic Structure **2020**, 2, 023002.
- (51) Gross, E. K. U.; Kohn, W. Local density-functional theory of frequency-dependent linear response. Phys. Rev. Lett. **1985**, 55, 2850–2852.
- (52) Quong, A. A.; Eguiluz, A. G. First-principles evaluation of dynamical response and plasmon dispersion in metals. Phys. Rev. Lett. **1993**, 70, 3955–3958.
- (53) Weissker, H.-C.; Serrano, J.; Huotari, S.; Bruneval, F.; Sottile, F.; Monaco, G.; Krisch, M.; Olevano, V.; Reining, L. Signatures of Short-Range Many-Body Effects in the Dielectric Function of Silicon for Finite Momentum Transfer. Phys. Rev. Lett. **2006**, 97, 237602.

- (54) Weissker, H.-C.; Serrano, J.; Huotari, S.; Luppi, E.; Cazzaniga, M.; Bruneval, F.; Sottile, F.; Monaco, G.; Olevano, V.; Reining, L. Dynamic structure factor and dielectric function of silicon for finite momentum transfer: Inelastic x-ray scattering experiments and ab initio calculations. Phys. Rev. B **2010**, 81, 085104.
- (55) Moldabekov, Z. A.; Lokamani, M.; Vorberger, J.; Cangi, A.; Dornheim, T. Non-empirical Mixing Coefficient for Hybrid XC Functionals from Analysis of the XC Kernel. The Journal of Physical Chemistry Letters **2023**, 14, 1326–1333.
- (56) Moldabekov, Z.; Böhme, M.; Vorberger, J.; Blaschke, D.; Dornheim, T. Ab Initio Static Exchange–Correlation Kernel across Jacob’s Ladder without Functional Derivatives. Journal of Chemical Theory and Computation **2023**, 19, 1286–1299.
- (57) Krane, K. Dispersion and damping of volume plasmons in polycrystalline aluminium and indium. Journal of Physics F: Metal Physics **1978**, 8, 2133.
- (58) Sprösser-Prou, J.; Vom Felde, A.; Fink, J. Aluminum bulk-plasmon dispersion and its anisotropy. Physical Review B **1989**, 40, 5799.
- (59) Brydson, R. Electron Energy Loss Spectroscopy; CRC Press, 2020.
- (60) Mortensen, J. J.; Hansen, L. B.; Jacobsen, K. W. Real-space grid implementation of the projector augmented wave method. Physical Review B **2005**, 71, 035109.
- (61) Enkovaara, J.; Rostgaard, C.; Mortensen, J. J.; Chen, J.; Duřak, M.; Ferrighi, L.; Gavnholt, J.; Glinsvad, C.; Haikola, V.; Hansen, H. A.; Kristoffersen, H. H.; Kuisma, M.; Larsen, A. H.; Lehtovaara, L.; Ljungberg, M.; Lopez-Acevedo, O.; Moses, P. G.; Ojanen, J.; Olsen, T.; Petzold, V.; Romero, N. A.; Stausholm-Møller, J.; Strange, M.; Tritsarlis, G. A.; Vanin, M.; Walter, M.; Hammer, B.; Häkkinen, H.; Madsen, G. K. H.; Nieminen, R. M.; Nørskov, J. K.; Puska, M.; Rantala, T. T.; Schiøtz, J.; Thygesen, K. S.; Jacobsen, K. W. Electronic structure calculations with GPAW: a real-

- space implementation of the projector augmented-wave method. Journal of Physics: Condensed Matter **2010**, 22, 253202.
- (62) Walter, M.; Häkkinen, H.; Lehtovaara, L.; Puska, M.; Enkovaara, J.; Rostgaard, C.; Mortensen, J. J. Time-dependent density-functional theory in the projector augmented-wave method. The Journal of Chemical Physics **2008**, 128, 244101.
- (63) Yan, J.; Mortensen, J. J.; Jacobsen, K. W.; Thygesen, K. S. Linear density response function in the projector augmented wave method: Applications to solids, surfaces, and interfaces. Phys. Rev. B **2011**, 83, 245122.
- (64) Larsen, A. H.; Mortensen, J. J.; Blomqvist, J.; Castelli, I. E.; Christensen, R.; Dułak, M.; Friis, J.; Groves, M. N.; Hammer, B.; Hargus, C.; Hermes, E. D.; Jennings, P. C.; Jensen, P. B.; Kermode, J.; Kitchin, J. R.; Kolsbjerg, E. L.; Kubal, J.; Kaasbjerg, K.; Lysgaard, S.; Maronsson, J. B.; Maxson, T.; Olsen, T.; Pastewka, L.; Peterson, A.; Rostgaard, C.; Schiøtz, J.; Schütt, O.; Strange, M.; Thygesen, K. S.; Vegge, T.; Vilhelmsen, L.; Walter, M.; Zeng, Z.; Jacobsen, K. W. The atomic simulation environment—a Python library for working with atoms. Journal of Physics: Condensed Matter **2017**, 29, 273002.
- (65) Bahn, S. R.; Jacobsen, K. W. An object-oriented scripting interface to a legacy electronic structure code. Computing in Science & Engineering **2002**, 4, 56–66.
- (66) Blöchl, P. E. Projector augmented-wave method. Phys. Rev. B **1994**, 50, 17953–17979.
- (67) Perdew, J. P.; Wang, Y. Accurate and simple analytic representation of the electron-gas correlation energy. Phys. Rev. B **1992**, 45, 13244–13249.
- (68) Wyckoff, R. W. G. Crystal Structures; Interscience Publishers: New York, 1948.
- (69) Sprösser-Prou, J.; vom Felde, A.; Fink, J. Aluminum bulk-plasmon dispersion and its anisotropy. Phys. Rev. B **1989**, 40, 5799–5801.

- (70) Mahan, G. Many-Particle Physics; Physics of Solids and Liquids; Springer US, 1990.
- (71) Bohm, D.; Gross, E. P. Theory of Plasma Oscillations. A. Origin of Medium-Like Behavior. Phys. Rev. **1949**, 75, 1851–1864.
- (72) Hamann, P.; Vorberger, J.; Dornheim, T.; Moldabekov, Z. A.; Bonitz, M. Ab initio results for the plasmon dispersion and damping of the warm dense electron gas. Contributions to Plasma Physics **2020**, 60, e202000147.
- (73) Ott, T.; Thomsen, H.; Abraham, J. W.; Dornheim, T.; Bonitz, M. Recent progress in the theory and simulation of strongly correlated plasmas: phase transitions, transport, quantum, and magnetic field effects. The European Physical Journal D **2018**, 72, 84.
- (74) Kraus, D.; Ravasio, A.; Gauthier, M.; Gericke, D. O.; Vorberger, J.; Frydrych, S.; Helfrich, J.; Fletcher, L. B.; Schaumann, G.; Nagler, B.; Barbrel, B.; Bachmann, B.; Gamboa, E. J.; Göde, S.; Granados, E.; Gregori, G.; Lee, H. J.; Neumayer, P.; Schumaker, W.; Döppner, T.; Falcone, R. W.; Glenzer, S. H.; Roth, M. Nanosecond formation of diamond and lonsdaleite by shock compression of graphite. Nature Communications **2016**, 7, 10970.
- (75) Lazicki, A.; McGonegle, D.; Rygg, J. R.; Braun, D. G.; Swift, D. C.; Gorman, M. G.; Smith, R. F.; Heighway, P. G.; Higginbotham, A.; Suggit, M. J.; Fratanduono, D. E.; Coppari, F.; Wehrenberg, C. E.; Kraus, R. G.; Erskine, D.; Bernier, J. V.; McNaney, J. M.; Rudd, R. E.; Collins, G. W.; Eggert, J. H.; Wark, J. S. Metastability of diamond ramp-compressed to 2 terapascals. Nature **2021**, 589, 532–535.
- (76) Kraus, D.; Bachmann, B.; Barbrel, B.; Falcone, R. W.; Fletcher, L. B.; Frydrych, S.; Gamboa, E. J.; Gauthier, M.; Gericke, D. O.; Glenzer, S. H.; Göde, S.; Granados, E.; Hartley, N. J.; Helfrich, J.; Lee, H. J.; Nagler, B.; Ravasio, A.; Schumaker, W.; Vorberger, J.; Döppner, T. Characterizing the ionization potential depression in dense

- carbon plasmas with high-precision spectrally resolved x-ray scattering. Plasma Phys. Control Fusion **2019**, 61, 014015.
- (77) Böhme, M. P.; Fletcher, L. B.; Döppner, T.; Kraus, D.; Baczewski, A. D.; Preston, T. R.; MacDonald, M. J.; Graziani, F. R.; Moldabekov, Z. A.; Vorberger, J.; Dornheim, T. Evidence of free-bound transitions in warm dense matter and their impact on equation-of-state measurements. 2023.
- (78) Kozłowski, J.; Perchak, D.; Kieron Burke, <https://arxiv.org/abs/2308.03319>. Generalized Gradient Approximation Made Thermal. arXiv **2023**,
- (79) Karasiev, V. V.; Dufty, J. W.; Trickey, S. B. Nonempirical Semilocal Free-Energy Density Functional for Matter under Extreme Conditions. Phys. Rev. Lett. **2018**, 120, 076401.
- (80) Karasiev, V. V.; Sjöstrom, T.; Dufty, J.; Trickey, S. B. Accurate Homogeneous Electron Gas Exchange-Correlation Free Energy for Local Spin-Density Calculations. Phys. Rev. Lett. **2014**, 112, 076403.
- (81) Groth, S.; Dornheim, T.; Sjöstrom, T.; Malone, F. D.; Foulkes, W. M. C.; Bonitz, M. Ab initio Exchange–Correlation Free Energy of the Uniform Electron Gas at Warm Dense Matter Conditions. Phys. Rev. Lett. **2017**, 119, 135001.
- (82) Dornheim, T.; Groth, S.; Bonitz, M. The uniform electron gas at warm dense matter conditions. Phys. Reports **2018**, 744, 1–86.
- (83) Karasiev, V. V.; Calderin, L.; Trickey, S. B. Importance of finite-temperature exchange correlation for warm dense matter calculations. Phys. Rev. E **2016**, 93, 063207.
- (84) Ramakrishna, K.; Dornheim, T.; Vorberger, J. Influence of finite temperature exchange-correlation effects in hydrogen. Phys. Rev. B **2020**, 101, 195129.

- (85) Dornheim, T.; Groth, S.; Vorberger, J.; Bonitz, M. Ab initio Path Integral Monte Carlo Results for the Dynamic Structure Factor of Correlated Electrons: From the Electron Liquid to Warm Dense Matter. Phys. Rev. Lett. **2018**, 121, 255001.